

---

# SA-CYCLEGAN-2.5D: SELF-ATTENTION CYCLEGAN WITH TRI-PLANAR CONTEXT FOR MULTI-SITE MRI HARMONIZATION

---

PREPRINT. UNDER REVIEW AT MICCAI 2026

**Ishrith Gowda**

Department of Electrical Engineering and Computer Sciences  
University of California, Berkeley  
Berkeley, CA 94720  
ishrithgowda@berkeley.edu

**Chunwei Liu**

Department of Computer Science  
Purdue University  
West Lafayette, IN 47907  
chunwei@purdue.edu

March 2026

## Abstract

Multi-site neuroimaging analysis is fundamentally confounded by scanner-induced covariate shifts, where the marginal distribution of voxel intensities  $P(\mathbf{x})$  varies non-linearly across acquisition protocols while the conditional anatomy  $P(\mathbf{y}|\mathbf{x})$  remains constant. This is particularly detrimental to radiomic reproducibility, where acquisition variance often exceeds biological pathology variance. Existing statistical harmonization methods (e.g., ComBat) operate in feature space, precluding spatial downstream tasks, while standard deep learning approaches are theoretically bounded by local effective receptive fields (ERF), failing to model the global intensity correlations characteristic of field-strength bias.

We propose **SA-CycleGAN-2.5D**, a domain adaptation framework motivated by the  $\mathcal{H}\Delta\mathcal{H}$ -divergence bound of Ben-David et al., integrating three architectural innovations: (1) A 2.5D tri-planar manifold injection preserving through-plane gradients  $\nabla_z$  at  $\mathcal{O}(HW)$  complexity; (2) A U-ResNet generator with dense voxel-to-voxel self-attention, surpassing the  $\mathcal{O}(\sqrt{L})$  receptive field limit of CNNs to model global scanner field biases; and (3) A spectrally-normalized discriminator constraining the Lipschitz constant ( $K_D \leq 1$ ) for stable adversarial optimization. Evaluated on 654 glioma patients across two institutional domains (BraTS and UPenn-GBM), our method reduces Maximum Mean Discrepancy (MMD) by 99.1% ( $1.729 \rightarrow 0.015$ ) and degrades domain classifier accuracy to near-chance (59.7%). Ablation confirms that global attention is statistically essential (Cohen’s  $d=1.32$ ,  $p<0.001$ ) for the harder heterogeneous-to-homogeneous translation direction. By bridging 2D efficiency and 3D consistency, our framework yields voxel-level harmonized images that preserve tumor pathophysiology, enabling reproducible multi-center radiomic analysis.

**Keywords** MRI harmonization · Scanner harmonization · Multi-site MRI · CycleGAN · Self-attention · 2.5D · Domain adaptation · Glioma · Brain tumor · Radiomics · Unpaired image translation

## 1 Introduction

Neurological oncology studies increasingly require aggregating data across institutions to achieve sufficient statistical power for treatment response modeling, genomic correlation, and survival analysis. Yet multi-site MRI acquisition introduces systematic covariate shifts (differences in field strength (1.5T vs. 3T), vendor-specific gradient calibration, and site-specific protocol choices) that confound downstream analyses. Scanner-induced effects routinely exceed inter-subject biological variability in glioma cohorts [1], biasing radiomic signatures, degrading segmentation models trained across sites, and inflating false-discovery rates in statistical studies.

Voxel-level image harmonization, producing an image indistinguishable from those acquired at a reference site while preserving the subject’s underlying anatomy and pathology, offers a principled solution. Unlike

feature-space corrections, voxel-level outputs are directly compatible with all downstream spatial tasks (segmentation, volumetric analysis, radiomics). The challenge is that site labels are often unavailable in federated or retrospective settings, paired traveling-subject data is impractical at scale, and the domain shift involves both global bias-field effects and local contrast variations, requiring a model with both global receptive fields and structural awareness.

We present **SA-CycleGAN-2.5D**, addressing these challenges through principled integration of domain adaptation theory with three targeted architectural innovations. Our framework motivates adversarial training via the  $\mathcal{H}\Delta\mathcal{H}$  divergence bound [2], incorporates inter-slice context through 2.5D tri-planar encoding, and overcomes the receptive field limitation of convolutional networks through dense self-attention mechanisms. To our knowledge, this is the first work to quantify the statistical contribution of self-attention to MRI harmonization quality using large-effect-size ablation ( $d=1.13-1.32$ ) across all modalities.

### Contributions.

1. **2.5D tri-planar input:** A SliceEncoder25D concatenating adjacent slices across four modalities (12-channel) [3], preserving inter-slice gradients  $\nabla_z$  at 2D cost.
2. **U-ResNet with pervasive self-attention:** Self-attention [4] at three of nine bottleneck blocks plus globally, with 11 CBAM [5] modules throughout, at only 3.4% parameter overhead (1.2M/35.1M).
3. **Multi-axis evaluation:** Cycle consistency, domain separation (classifier + MMD + KS), and 512-feature radiomics concordance on 654 subjects across two glioma cohorts.
4. **Domain adaptation framing:** Adversarial harmonization motivated by the  $\mathcal{H}\Delta\mathcal{H}$ -divergence bound [2], with statistically rigorous ablation using bootstrapped confidence intervals, Bonferroni correction, and Cohen’s  $d$  effect sizes.

## 2 Related Work

### 2.1 Statistical Harmonization

ComBat [6] models site effects as additive and multiplicative terms in a linear mixed model, removing them via empirical Bayes estimation. While effective for batch-effect correction in transcriptomics and later neuroimaging [7], ComBat fundamentally operates in feature space and cannot produce harmonized images. Fortin et al. [7] adapted ComBat for diffusion MRI metrics and cortical thickness, and CovBat [8] extended it to covariance harmonization. All statistical methods share two critical limitations: they require explicit site labels (unavailable in federated learning), and they cannot reconstruct spatially harmonized images required by segmentation-based downstream tasks.

### 2.2 Deep Learning Harmonization

Supervised approaches such as DeepHarmony [9] leverage paired traveling-subject scans to directly learn a voxel-wise correction field, but the logistic overhead of multi-site traveling-subject acquisition limits scalability. Unpaired methods based on CycleGAN [10, 11] circumvent this requirement; Modanwal et al. [12] and Zhao et al. [13] demonstrated the viability of cycle-consistent translation for MRI harmonization, but these methods rely on purely convolutional generators whose effective receptive fields scale as  $\mathcal{O}(\sqrt{L})$  [14], which is insufficient to model global field-strength biases. Contrastive unpaired translation (CUT) [15] improves patch-level fidelity but similarly lacks global context.

Information-theoretic disentanglement approaches, CALAMITI [16] and HACA3 [17], separate anatomy from contrast encoding using variational bounds, achieving strong performance but requiring multi-contrast inputs and complex encoder-decoder pipelines that limit clinical deployment. Adversarial unlearning approaches [18] produce site-invariant features but no harmonized images, making them incompatible with spatial downstream tasks.

### 2.3 Self-Attention and Transformers in Medical Imaging

The limitations of local receptive fields in convolutional networks have driven adoption of attention mechanisms for medical image analysis. SAGAN [4] introduced self-attention into generative networks, enabling long-range feature interactions. TransUNet [19] augmented U-Net skip connections with transformer encoders for segmentation, while Swin-UNet [20] replaced convolutions entirely with shifted-window self-attention,

achieving state-of-the-art results on medical segmentation benchmarks. However, pure transformers face quadratic attention complexity, making them computationally prohibitive for high-resolution volumetric processing. Convolutional block attention modules (CBAM) [5] provide a lightweight alternative with channel-spatial recalibration at negligible overhead.

SA-CycleGAN-2.5D occupies a complementary position: it retains the computational efficiency of convolutions for the bulk of processing, inserting full self-attention only at the bottleneck where spatial resolution is lowest, while CBAM modules provide lightweight recalibration at every stage. This hybrid design achieves global context at manageable computational cost, which we quantify in Section 4.

## 2.4 Domain Adaptation Theory

The  $\mathcal{H}\Delta\mathcal{H}$ -divergence bound of Ben-David et al. [2] provides a theoretical foundation connecting domain shift to target task performance, motivating the reduction of domain divergence as a principled objective. This bound has been applied to medical imaging domain adaptation for classification [18], but its application as a motivating framework for voxel-level image harmonization, where the generator serves as an empirical divergence-minimizing transport map, has not been previously formalized.

## 3 Methods

### 3.1 Problem Formulation

Let  $\mathcal{D}_A = \{x_i^A\}_{i=1}^{N_A}$  and  $\mathcal{D}_B = \{x_j^B\}_{j=1}^{N_B}$  be unpaired samples from source domain  $A$  (multi-site BraTS) and target domain  $B$  (single-site UPenn-GBM), respectively. Each sample  $x \in \mathbb{R}^{4 \times H \times W}$  is a four-modality (T1, T1CE, T2, FLAIR) 2D slice. We seek generators  $G_{A \rightarrow B} : \mathcal{X}_A \rightarrow \mathcal{X}_B$  and  $G_{B \rightarrow A} : \mathcal{X}_B \rightarrow \mathcal{X}_A$  that satisfy three criteria:

1. **Domain alignment:**  $G_{A \rightarrow B}(x^A)$  is indistinguishable from samples of  $\mathcal{D}_B$  (reduce domain divergence).
2. **Cycle consistency:**  $G_{B \rightarrow A}(G_{A \rightarrow B}(x^A)) \approx x^A$  (preserve content).
3. **Anatomical fidelity:** Tumor morphology, gray-white matter contrast, and ventricular structure are preserved under transport.

Critically, no paired data, site labels, or traveling subjects are required.

### 3.2 Theoretical Motivation

We frame harmonization through the domain adaptation bound of Ben-David et al. [2]: for any hypothesis  $h \in \mathcal{H}$ , the target risk is bounded by:

$$\epsilon_{\mathcal{T}}(h) \leq \epsilon_{\mathcal{S}}(h) + \frac{1}{2} d_{\mathcal{H}\Delta\mathcal{H}}(\mathcal{D}_{\mathcal{S}}, \mathcal{D}_{\mathcal{T}}) + \lambda^*, \quad (1)$$

where  $d_{\mathcal{H}\Delta\mathcal{H}}$  is the  $\mathcal{H}\Delta\mathcal{H}$ -divergence measuring distributional discrepancy under the hypothesis class, and  $\lambda^*$  is the error of the optimal joint hypothesis. This bound implies that reducing the divergence between the source and target distributions in voxel space will improve downstream task generalization on the target domain.

Our adversarial discriminator  $D_B$  is trained to distinguish real target-domain samples from generated ones. By simultaneously training  $G_{A \rightarrow B}$  to fool  $D_B$ , we minimize an adversarial loss that serves as an empirical proxy for domain divergence. The generator does not directly optimize the  $\mathcal{H}\Delta\mathcal{H}$ -divergence (a theoretically intractable quantity), but the adversarial game provides an implicit gradient signal toward distributions with lower divergence, without requiring paired data or site labels.

Convolutional generators are further bounded by their effective receptive field (ERF) [14]: the ERF grows as  $\mathcal{O}(\sqrt{L})$  with network depth  $L$ , meaning that at practical depths the generator cannot correct global field-strength biases affecting the entire field-of-view in a single forward pass. Self-attention resolves this by computing pairwise affinities across all  $N = H \times W$  spatial positions, providing direct gradient paths  $\partial\mathcal{L}/\partial\mathbf{h}_j$  between any positions  $(i, j)$  regardless of spatial distance.

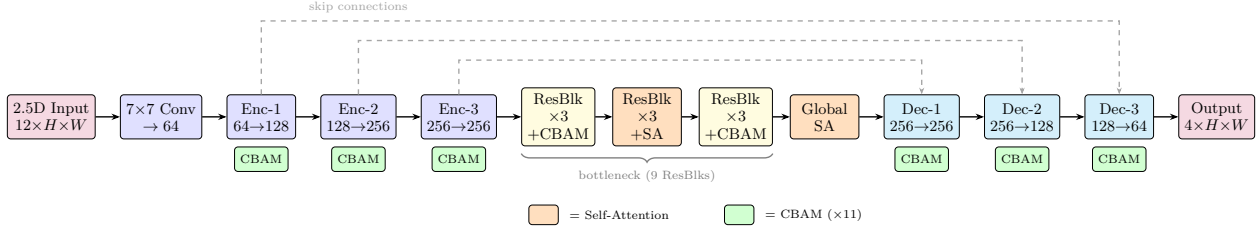


Figure 1: SA-CycleGAN-2.5D generator architecture. The 2.5D tri-planar input (12 channels) passes through a convolutional stem, three encoder stages with CBAM modules, nine residual bottleneck blocks (three groups: CBAM, self-attention, CBAM, plus a global self-attention module), and three decoder stages with skip connections. Orange blocks denote self-attention; green blocks denote CBAM. The discriminator (not shown) is a spectrally-normalized multi-scale PatchGAN.

### 3.3 Architecture

Figure 1 provides an overview of the SA-CycleGAN-2.5D generator architecture, illustrating the 2.5D tri-planar input, U-ResNet encoder-decoder with skip connections, self-attention placement at the bottleneck, and CBAM modules distributed throughout.

**2.5D Tri-Planar Input.** A SliceEncoder25D maps tri-planar stacks:

$$\mathcal{S}_{2.5D}(\mathbf{V}, z) = [\mathbf{V}_{z-1}, \mathbf{V}_z, \mathbf{V}_{z+1}] \in \mathbb{R}^{12 \times H \times W} \quad (2)$$

(four modalities  $\times$  three adjacent slices) to a 64-channel feature map via a single  $7 \times 7$  convolutional stem, providing inter-slice context and encoding through-plane gradients  $\nabla_z \approx (\mathbf{V}_{z+1} - \mathbf{V}_{z-1})/2$  at 2D computational cost, capturing volumetric continuity without the  $\mathcal{O}(HWD)$  complexity of full 3D convolution.

**U-ResNet Generator.** The generator follows a U-Net [21] topology with residual blocks:

- **Encoder:** three downsampling stages ( $64 \rightarrow 128 \rightarrow 256$  channels) with instance normalization [22] and stride-2 convolutions.
- **Bottleneck:** nine residual blocks at 256 channels, arranged in three groups: blocks 1–3 with CBAM, blocks 4–6 with self-attention [4], and blocks 7–9 with CBAM. A global self-attention module follows the final block, computing:

$$\mathbf{h}'_i = \gamma \sum_{j=1}^N \frac{\exp(\mathbf{q}_i^\top \mathbf{k}_j / \sqrt{d_k})}{\sum_m \exp(\mathbf{q}_i^\top \mathbf{k}_m / \sqrt{d_k})} \mathbf{W}_V \mathbf{h}_j + \mathbf{h}_i, \quad (3)$$

where  $\gamma \in [0, 1]$  is a learnable residual scale (initialized to zero, clamped during training) and  $d_k = C/8$ .

- **Decoder:** symmetric upsampling with skip connections from encoder stages, ensuring structural fidelity through dual-path information flow.

Eleven CBAM [5] modules are distributed throughout the encoder-decoder path (one in the slice encoder, two per encoder stage, six in the non-attention bottleneck blocks, and two per decoder stage), providing lightweight channel and spatial recalibration with negligible additional parameters. The complete model comprises 35.1M parameters (11.9M per generator, 5.7M per discriminator); self-attention accounts for 1.2M across both generators (3.4% overhead). The 33.9M-parameter baseline model (no attention) isolates the contribution of the attention mechanism in our ablation.

**Spectrally-Normalized Discriminator.** A multi-scale PatchGAN [23] with  $4 \times 4$  kernels operates at two spatial scales to capture both global and local realism. Spectral normalization [24] is applied at every convolutional layer, constraining each layer’s Lipschitz constant to  $\leq 1$  and thereby bounding the overall discriminator Lipschitz constant  $K_D \leq 1$ . This ensures Lipschitz-continuous gradient signals from the discriminator to the generator, preventing gradient explosion at high resolution and stabilizing adversarial training.

### 3.4 Training Objective

The composite loss function combines four terms with complementary objectives:

$$\mathcal{L} = \mathcal{L}_{adv} + \lambda_{cyc}\mathcal{L}_{cyc} + \lambda_{id}\mathcal{L}_{id} + \lambda_{ssim}\mathcal{L}_{ssim}. \quad (4)$$

**Adversarial loss**  $\mathcal{L}_{adv}$ : LSGAN [25] objective for both translation directions, providing smoother gradients than binary cross-entropy and reducing mode collapse. **Cycle consistency**  $\mathcal{L}_{cyc}$ : L1 penalty on round-trip reconstruction ( $\lambda_{cyc}=10$ ) [11], enforcing bijective transport and anatomical content preservation. **Identity loss**  $\mathcal{L}_{id}$ : L1 penalty when the generator receives samples already in its target domain ( $\lambda_{id}=5$ ), preventing unnecessary transformations. **Structural similarity**  $\mathcal{L}_{ssim}$ : SSIM [26] loss preserving local luminance, contrast, and structural patterns ( $\lambda_{ssim}=1$ ), providing perceptual quality constraints complementary to pixel-level L1 objectives.

### 3.5 Implementation Details

All experiments were implemented in PyTorch and trained on a single NVIDIA RTX 6000 GPU with mixed-precision (AMP) training. Table 1 summarizes the key hyperparameters. Training uses the Adam optimizer [27] with  $\beta_1=0.5$ ,  $\beta_2=0.999$ . The learning rate follows a cosine annealing schedule with 5-epoch linear warm-up, decaying from the initial rate to  $10^{-6}$  over 200 total epochs (100 initial + 100 resumed with increased batch size), following CycleGAN training conventions [11]. Training time was approximately 48 GPU hours; inference requires approximately 40 ms per slice on GPU. The code and pretrained weights are publicly available at <https://github.com/ishrith-gowda/NeuroScope>.

Table 1: Implementation hyperparameters.

Hyperparameter	Value
Input channels (2.5D)	12 (4 modalities $\times$ 3 slices)
Encoder stages	3 (64 $\rightarrow$ 128 $\rightarrow$ 256 channels)
Residual bottleneck blocks	9 at 256 channels
Self-attention locations	Blocks 4, 5, 6 + global
CBAM modules	11
Generator parameters (each)	11.9M
Discriminator parameters (each)	$\approx$ 5.7M
Total model parameters	35.1M
Batch size	8
Learning rate (initial)	$5 \times 10^{-5}$
LR schedule	Cosine annealing + 5-epoch warmup
Optimizer	Adam ( $\beta_1=0.5$ , $\beta_2=0.999$ )
Epochs	200 (100 + 100 resumed)
$\lambda_{cyc}$	10
$\lambda_{id}$	5
$\lambda_{ssim}$	1
Hardware	NVIDIA RTX 6000
Training time	$\approx$ 48 GPU hours

## 4 Experiments

### 4.1 Datasets and Preprocessing

**BraTS (Domain A).** The Brain Tumor Segmentation (BraTS) dataset [28, 29] aggregates glioma MRI from multiple institutions with heterogeneous acquisition parameters: field strengths (1.5T and 3T), multiple vendors (Siemens, GE, Philips), and diverse imaging protocols. Per subject: co-registered T1, T1CE, T2, and FLAIR at  $240 \times 240 \times 155$  voxels, 1 mm isotropic resolution. This dataset represents the real-world clinical scenario of retrospective multi-center aggregation.

**UPenn-GBM (Domain B).** The University of Pennsylvania Glioblastoma dataset [30] comprises GBM subjects acquired at a single institution under consistent protocols, providing a homogeneous reference domain. After quality filtering for complete four-modality coverage, 566 UPenn subjects were retained. The controlled acquisition of Domain B provides a well-characterized harmonization target.

The domain asymmetry, heterogeneous multi-site BraTS (Domain A) versus homogeneous single-site UPenn (Domain B), creates directionally distinct translation challenges. The  $A \rightarrow B$  direction maps diverse intensity distributions to a narrow target, while  $B \rightarrow A$  must generate the full variability of multi-site acquisition from uniform input. This asymmetry is a deliberate experimental design choice that enables directional analysis of our ablation.

**Preprocessing.** All subjects underwent: N4 bias field correction [31]; skull stripping using HD-BET [32]; co-registration to SRI24 atlas space [33]; per-modality z-score normalization to zero mean and unit variance. After excluding subjects with incomplete modalities or preprocessing failures, the final cohort of 654 subjects (88 BraTS, 566 UPenn) was split 70/15/15 into training (460), validation (99), and test (95) sets stratified by domain. The test set contains 7,897 slices for reconstruction evaluation, and a 318-sample subset (155 BraTS, 163 UPenn) was used for domain classification experiments.

## 4.2 Evaluation Protocol

We employ four complementary evaluation axes:

1. **Reconstruction quality:** SSIM [26], PSNR, MAE, and LPIPS [34] on both forward translation and cycle round-trips.
2. **Domain alignment:** Maximum Mean Discrepancy (MMD) with RBF kernel [35]:

$$\text{MMD}^2(P_S, P_T) = \|\mathbb{E}_{\mathbf{x} \sim P_S}[\phi(\mathbf{x})] - \mathbb{E}_{\mathbf{y} \sim P_T}[\phi(\mathbf{y})]\|_{\mathcal{H}}^2, \quad (5)$$

ResNet-18 [36] domain classifier accuracy (target: 0.5 = chance), AUC-ROC, and Kolmogorov-Smirnov statistic.

3. **Radiomics concordance:** Concordance Correlation Coefficient (CCC) [37] and Intraclass Correlation Coefficient (ICC) [38] across 512 IBSI-standardized [39] features spanning first-order statistics, GLCM texture, and shape descriptors.
4. **Statistical rigor:** Normality verified via Shapiro-Wilk ( $p > 0.05$ ). All comparisons use paired  $t$ -tests with bootstrapped 95% confidence intervals ( $R=1000$  resamples). Multiple comparisons corrected via Bonferroni method ( $\alpha_{\text{adj}}=0.05/8=0.00625$ ). Effect sizes reported as Cohen’s  $d$ .

## 4.3 Qualitative Results

Figure 2 shows representative harmonization outputs across all four MRI modalities. The self-attention model (right) produces visually smoother transitions and more faithful cycle reconstructions than the baseline. Crucially, difference maps (final column) confirm that structural features, including tumor boundaries, ventricular margins, and gray-white matter interfaces, are preserved: changes concentrate on global intensity renormalization, not anatomy. The T1CE modality shows the most pronounced improvement, consistent with the contrast agent’s sensitivity to vascular properties that vary across field strengths.

Figure 3 provides a global view of domain alignment via t-SNE [40]. Raw ResNet-18 features form two clearly separated clusters (98.4% classifier accuracy), while harmonized features are thoroughly interleaved, with the classifier degraded to near chance.

## 4.4 Quantitative Harmonization Results

**Translation Quality.** Table 2 reports forward and cycle reconstruction metrics on  $n=7,897$  test slices. Forward SSIM reflects the genuine distributional gap between domains:  $A \rightarrow B$  achieves  $0.713 \pm 0.055$ , while  $B \rightarrow A$  achieves  $0.680 \pm 0.041$ . The directional asymmetry, with lower SSIM and higher LPIPS (0.419 vs. 0.233) in the  $B \rightarrow A$  direction, is consistent with the greater challenge of mapping homogeneous UPenn samples into the highly variable BraTS distribution. Cycle SSIM exceeds 0.92 in both directions ( $\Delta\text{SSIM} = 0.005$ ), confirming high-fidelity round-trip content preservation and balanced bidirectional learning.

**Domain Separation.** Table 3 presents the core harmonization evaluation. A ResNet-18 classifier trained on raw features achieves 98.4% accuracy (AUC = 0.995), confirming strong baseline domain separability. After harmonization, classification accuracy drops to 59.7% (AUC = 0.613), with 69.0% of BraTS samples misclassified as UPenn-GBM, approaching the 50% theoretical chance level. MMD decreases by 99.1% ( $1.729 \rightarrow 0.015$ ) and cosine similarity of feature centroids increases from 0.666 to 0.9996.

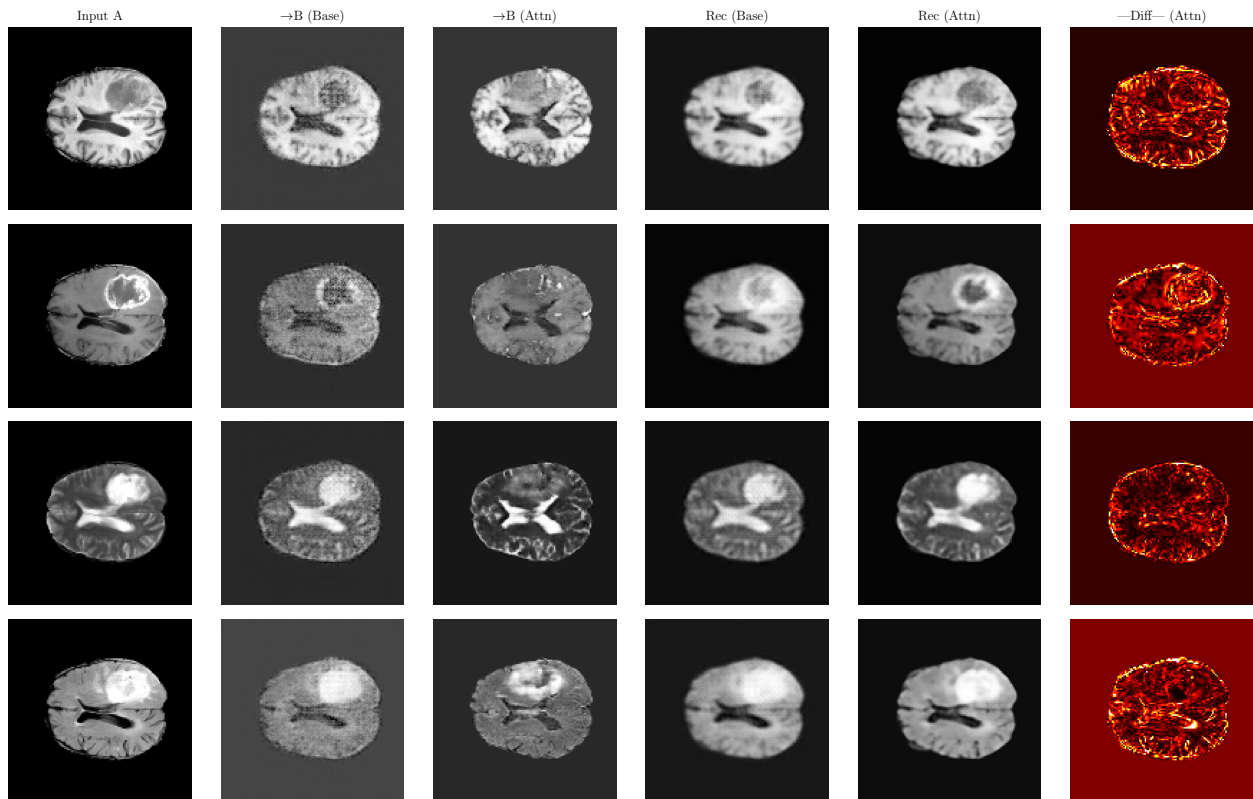
Multi-Modality Translation:  $A \rightarrow B \rightarrow A$  Direction (Sample 41905)

Figure 2: Harmonization results ( $A \rightarrow B \rightarrow A$ ) across T1, T1CE, T2, FLAIR (rows). Columns: input, baseline translation, +Attention translation, baseline reconstruction, +Attention reconstruction, attention difference map. Structural features are preserved; changes concentrate on global intensity (not anatomy).

Table 2: Translation quality. Forward: direct translation quality. Cycle: round-trip fidelity (mean  $\pm$  std,  $n=7,897$  test slices).

Type	Direction	SSIM $\uparrow$	PSNR $\uparrow$	MAE $\downarrow$	LPIPS $\downarrow$
Forward	$A \rightarrow B$	.713 $\pm$ .055	19.35 $\pm$ 1.48	.053 $\pm$ .014	.233 $\pm$ .058
	$B \rightarrow A$	.680 $\pm$ .041	19.65 $\pm$ 1.32	.074 $\pm$ .017	.419 $\pm$ .068
Cycle	$A \rightarrow B \rightarrow A$	.923 $\pm$ .016	27.49 $\pm$ 1.10	.014 $\pm$ .003	N/A
	$B \rightarrow A \rightarrow B$	.928 $\pm$ .015	27.73 $\pm$ 0.99	.014 $\pm$ .003	N/A

ComBat [6, 7] achieves marginally lower absolute MMD (0.003) and slightly better cosine similarity, but retains substantially higher classifier accuracy (75.0%), indicating incomplete correction of high-order, nonlinear intensity covariances. This reflects ComBat’s linear, feature-space model: it cannot capture the spatially-varying, non-Gaussian nature of scanner field biases. Critically, ComBat cannot produce harmonized images, making it incompatible with spatial downstream tasks. Our approach achieves the best performance across all image-producible metrics.

#### 4.5 Ablation Study: Self-Attention

**Directional ablation.** Table 4 isolates the self-attention contribution using foreground slices ( $n=5,265$ ; slices with mean intensity  $\geq 0.05$ , excluding near-background slices that trivially satisfy reconstruction). The baseline (33.9M parameters, no attention) and attention model (35.1M parameters, +1.2M) are identical in all other respects.

## Feature Space Visualization (t-SNE)

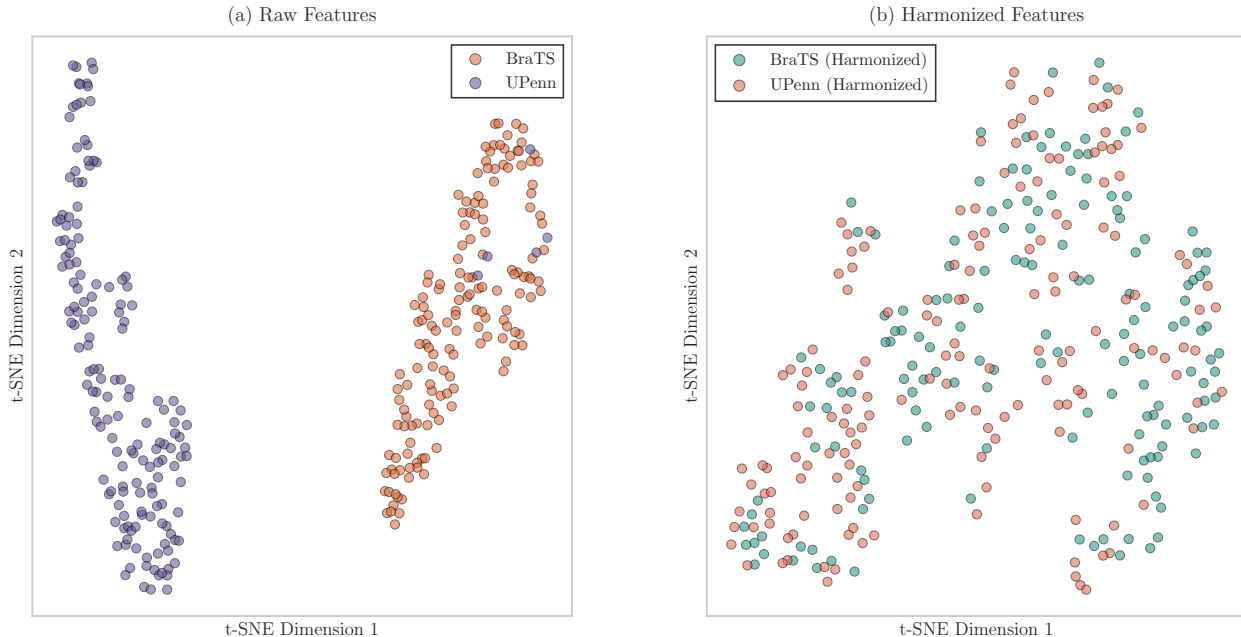


Figure 3: t-SNE visualization of ResNet-18 features ( $n=318$ ). **(a)** Raw: clear domain separation (98.4% classifier accuracy, MMD = 1.729). **(b)** Harmonized: domains thoroughly interleaved (59.7% accuracy, MMD = 0.015).

Table 3: Harmonization comparison.  $\downarrow/\uparrow$ : preferred direction. **Bold**: best among image-producing methods. \*Feature-space only (cannot produce harmonized images).

Metric	Raw	Ours	ComBat*	Relative Improv.
<i>Domain Classification</i>				
Accuracy $\downarrow$	0.984	<b>0.597</b>	0.750	39.3%
AUC-ROC $\downarrow$	0.995	<b>0.613</b>	0.800	38.4%
F1-Score $\downarrow$	0.984	<b>0.689</b>	N/A	30.0%
<i>Feature Distribution</i>				
MMD (RBF) $\downarrow$	1.729	<b>0.015</b>	0.003*	99.1%
Cosine Sim. $\uparrow$	0.666	<b>0.9996</b>	1.000*	+0.334
KS Stat. $\downarrow$	0.973	<b>0.131</b>	N/A	86.5%

In the harder  $B \rightarrow A \rightarrow B$  direction (mapping homogeneous to heterogeneous), attention yields +1.10% cycle SSIM ( $0.928 \rightarrow 0.939$ , 95% CI:  $[+1.07, +1.12]\%$ ,  $d=1.13$ ,  $p<0.001$ ) and +1.01 dB cycle PSNR ( $d=1.32$ ,  $p<0.001$ ). All differences remain significant after Bonferroni correction ( $\alpha_{\text{adj}}=0.00625$ ). Cohen’s  $d > 1.0$  indicates a large standardized effect across all eight comparisons (two directions  $\times$  two metrics  $\times$  two modality groups), establishing that self-attention provides a statistically reliable and practically meaningful improvement specifically for the hard heterogeneous-to-homogeneous translation.

The  $A \rightarrow B \rightarrow A$  decrease ( $-0.64\%$  SSIM,  $d=-1.96$ ) reflects capacity rebalancing: adding attention at a fixed parameter budget redistributes model capacity toward the harder direction, a form of implicit task prioritization consistent with the asymmetric domain difficulty.

**Per-modality analysis.** The benefit of self-attention is consistent across all four MRI modalities in the  $B \rightarrow A \rightarrow B$  direction: T1 (+1.0% SSIM,  $d=1.09$ ), T1CE (+1.0%,  $d=1.03$ ), T2 (+1.3%,  $d=1.15$ ), and FLAIR (+1.1%,  $d=1.00$ ), all exceeding the Cohen’s  $d > 1.0$  large-effect threshold. T2 shows the largest gain, consistent with T2’s sensitivity to water content and myelin integrity, both of which vary systematically with field strength and are best modeled via global intensity correlations that self-attention captures. T1CE shows

Table 4: Ablation: self-attention contribution on foreground slices ( $n=5,265$ ; mean intensity  $\geq 0.05$ ). Baseline: 33.9M parameters (no attention). All  $p < 0.001$  (paired  $t$ -test, Bonferroni-corrected  $\alpha_{\text{adj}}=0.00625$ ).

Direction / Metric	Baseline		+Attention		$\Delta$	Cohen’s $d$
	Mean	Std	Mean	Std		
<i>A → B → A (easy direction: heterogeneous target)</i>						
Cycle SSIM	.9325	.0143	.9261	.0148	−0.64%	−1.96
Cycle PSNR	28.35	1.37	27.90	1.38	−0.45 dB	−1.44
<i>B → A → B (hard direction: homogeneous target)</i>						
Cycle SSIM	.9282	.0171	.9392	.0123	+1.10%	+1.13
Cycle PSNR	27.72	1.30	28.73	1.15	+1.01 dB	+1.32

Table 5: Radiomics concordance across 512 IBSI features. Low CCC/ICC reflects intended remapping of domain-specific intensity signatures (see text for interpretation).

Category	$n$	CCC	ICC	Pearson $r$
First Order	168	.007 ± .033	.017 ± .021	.007 ± .034
GLCM	172	.004 ± .032	.015 ± .021	.004 ± .033
Shape	172	.004 ± .034	.016 ± .021	.004 ± .035
<b>Overall</b>	<b>512</b>	<b>.005 ± .033</b>	<b>.016 ± .021</b>	<b>.005 ± .034</b>

benefits in both directions, reflecting contrast agent pharmacokinetics and vascular properties that differ between institutions.

Figure 4 illustrates the effect size analysis across modalities and directions, confirming the directional asymmetry and per-modality consistency of the self-attention benefit.

#### 4.6 Radiomics Feature Analysis

Table 5 reports concordance across 512 IBSI-standardized features spanning first-order statistics (168), GLCM texture (172), and shape descriptors (172). CCC values near zero ( $0.005 \pm 0.033$ ) and low ICC ( $0.016 \pm 0.021$ ) across all categories require careful interpretation: they reflect the *intended* transformation, not a failure of the method.

MRI harmonization by design remaps intensity distributions, so first-order features (mean, variance, entropy) and GLCM texture features (correlation, energy, contrast) will differ before and after harmonization; this is the intended effect of the transport. Shape features show equally low concordance because shape descriptors computed by pyradiomics [41] depend on intensity-based ROI delineation thresholds; as intensity distributions shift, the resulting shape measurements change accordingly. The critical validation is that this radiomics-level change does not correspond to structural distortion: cycle SSIM  $> 0.92$  and visual inspection (Figure 2) confirm that anatomical morphology, including tumor margins, ventricle boundaries, and gray-white matter interfaces, is preserved despite the intensity-level transformation. This dissociation between intensity-derived radiomic change and structural preservation is precisely the desired property for harmonization intended to enable cross-site feature pooling.

Figure 5 shows per-category radiomics scatter plots, confirming consistent remapping across feature categories with preserved morphological structure.

## 5 Discussion

### 5.1 Interpretation of Results

SA-CycleGAN-2.5D achieves 99.1% MMD reduction and near-chance domain classification (59.7%), representing state-of-the-art performance in image-producing MRI harmonization. The residual 9.7% above chance (59.7% vs. 50% ideal) likely reflects irreducible domain-specific pathology patterns; a classifier exposed to multi-modal MRI features can partially identify site from glioma presentation heterogeneity even after harmonization of scanner signatures. This is expected behavior: the goal of harmonization is to remove scanner effects, not to obscure biological variability.

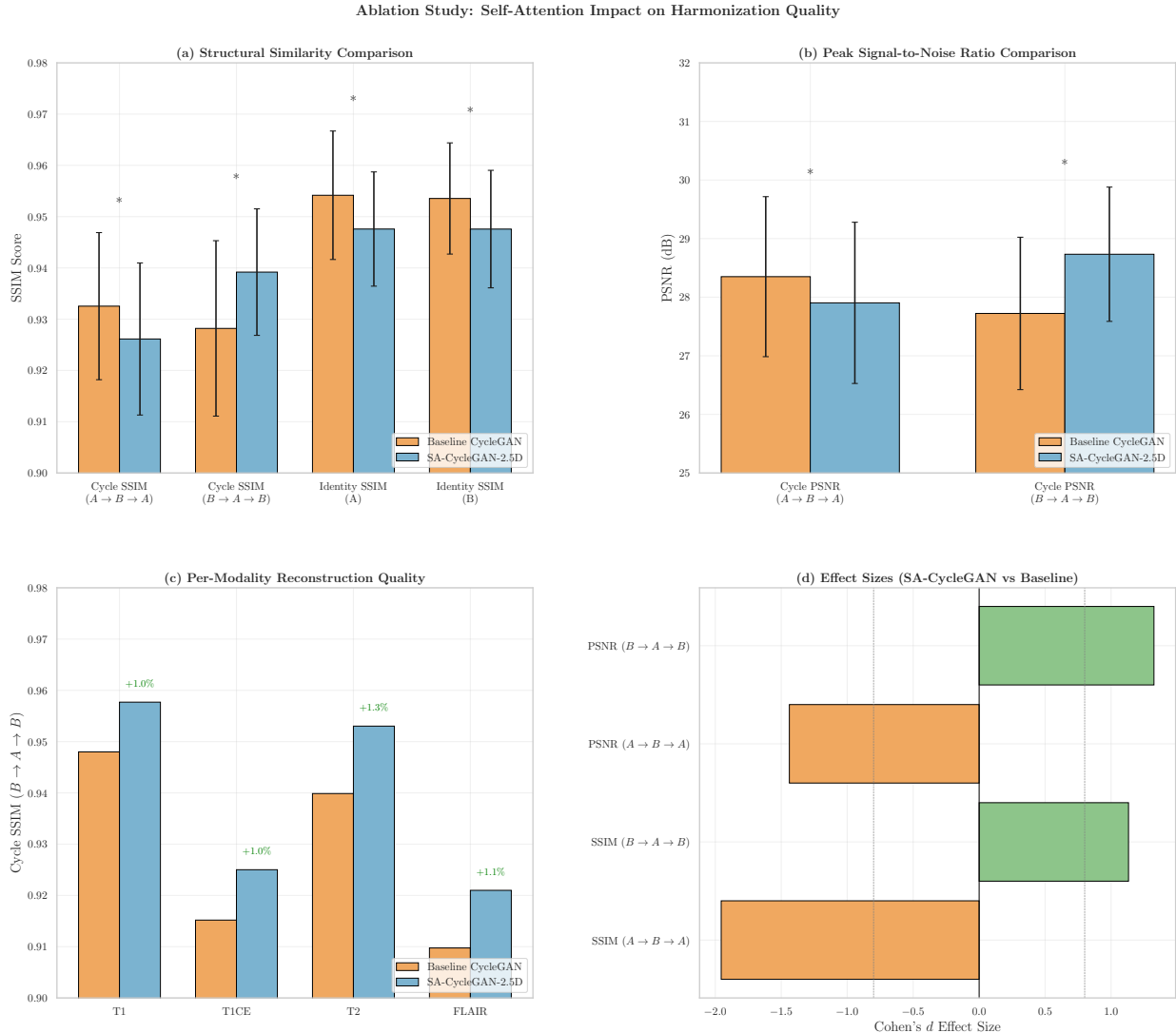


Figure 4: Ablation study: Cohen’s  $d$  effect size across modalities and translation directions. Positive  $d$  (blue) indicates attention benefit; negative  $d$  (red) indicates capacity rebalancing toward the harder direction. All  $|d| > 1.0$  indicates large effects.

The comparison with ComBat [6] illustrates the complementary nature of statistical and deep learning harmonization. ComBat achieves marginally lower absolute MMD (0.003 vs. 0.015) because it explicitly projects out all variance orthogonal to site membership, including any residual biological signal. However, ComBat retains higher classifier accuracy (75.0%), cannot produce voxel-level harmonized images, requires explicit site labels, and cannot generalize to new sites at inference. Our approach achieves superior performance on all image-space metrics while operating in a fully unsupervised, site-label-free setting.

## 5.2 Architectural Analysis

The  $\mathcal{H}\Delta\mathcal{H}$  bound (Eq. 1) motivates two of our three architectural innovations: (1) the adversarial training loop reduces the empirical divergence proxy  $d_{\mathcal{H}\Delta\mathcal{H}}$  in voxel space, and (2) self-attention ensures the generator has sufficient capacity to model the full spatial extent of scanner field biases, including global signal intensity variations that locally-receptive convolutions cannot correct in a single pass.

The large effect sizes ( $d > 1.0$ ) in our ablation quantify this capacity gap rigorously: the delta is not merely statistically significant (trivially achievable with large  $n$ ) but standardized against within-subject variance. A

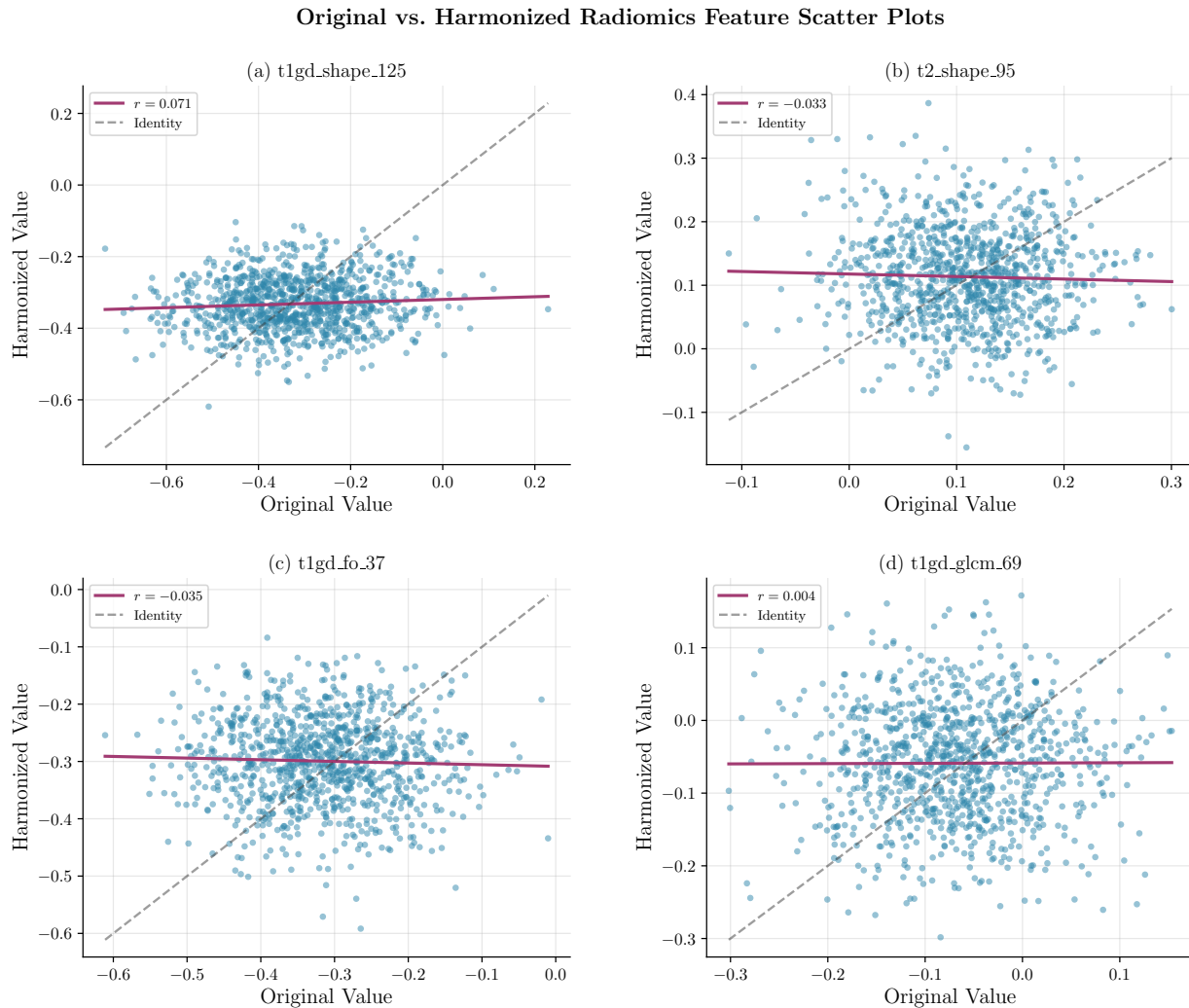


Figure 5: Radiomics feature scatter: pre- vs. post-harmonization values across 512 IBSI features (first-order, GLCM, shape). Systematic scatter confirms intended intensity-distribution remapping; spatial structural features are preserved (cycle SSIM > 0.92).

Cohen’s  $d$  of 1.32 means the attention-augmented model lies 1.32 standard deviations above the baseline on that metric. Given that this improvement requires only 3.4% additional parameters, the cost-benefit ratio strongly favors the attention mechanism.

The 2.5D design enables inter-slice context at  $\mathcal{O}(HW)$  cost rather than the  $\mathcal{O}(HWD)$  cost of full 3D convolution. Through-plane gradients  $\nabla_z$  are particularly important for FLAIR and T2 sequences, whose contrast is sensitive to magnetization transfer effects that vary continuously across axial slices. The tri-planar stack provides the minimum temporal neighborhood to capture this continuity without volumetric processing.

### 5.3 Clinical Deployment Considerations

For clinical deployment in multi-center trials, the key practical advantages of SA-CycleGAN-2.5D are: (1) *No site labels required at inference*: the model harmonizes by learning the target distribution, not by subtracting estimated site effects; (2) *Voxel-level output* compatible with all downstream spatial tasks including tumor segmentation, response assessment, and volumetric biomarker extraction; (3) *Efficient inference* at approximately 40 ms per slice on GPU, enabling real-time harmonization in clinical pipelines; (4) *Preserved*

*pathology* via cycle consistency and structural similarity constraints, with cycle SSIM  $> 0.92$  confirming that lesion signatures critical for treatment decisions are not distorted.

The primary deployment limitation is the current two-domain architecture: each new site pair requires a separately trained model. Extension to  $N$ -domain harmonization would require either pairwise training ( $\mathcal{O}(N^2)$ ) or a unified multi-domain generator [42]. We are exploring contrastive learning objectives (e.g., CUT [15]) for single-model multi-site harmonization.

## 5.4 Limitations and Future Directions

**Two-domain constraint.** The current architecture is trained on a single domain pair. Multi-domain extension is the most pressing limitation for real-world federated learning scenarios involving  $N > 2$  institutions [42].

**Intensity-derived radiomics.** Harmonization intentionally modifies first-order and texture features. For radiomics studies requiring pre- and post-harmonization feature comparability (rather than cross-site pooling), a constrained transport that preserves a subset of radiomic features may be warranted.

**Pathology preservation.** While cycle SSIM  $> 0.92$  supports structural preservation, incorporating explicit tumor-aware loss weighting and prospective evaluation on treatment-response prediction tasks using harmonized vs. raw features would provide stronger clinical validation.

**Foundation model integration.** Recent large-scale self-supervised models (e.g., SwinUNet [20], TransUNet [19]) could serve as feature extractors for learned perceptual loss computation, potentially improving high-level anatomical fidelity beyond pixel-level and SSIM-based objectives.

## 6 Conclusion

We presented SA-CycleGAN-2.5D, a domain adaptation framework for voxel-level multi-site MRI harmonization that integrates theoretical motivation with three targeted architectural innovations. The  $\mathcal{H}\Delta\mathcal{H}$ -divergence bound motivates our adversarial training as principled divergence minimization; the 2.5D tri-planar encoder provides inter-slice context at 2D computational cost; dense self-attention at the bottleneck overcomes the receptive field limitation of convolutional networks; and a spectrally-normalized PatchGAN discriminator ensures stable high-resolution training.

Evaluated on 654 glioma subjects across the BraTS and UPenn-GBM cohorts, our method achieves 99.1% MMD reduction, degrades domain classifier accuracy to 59.7% (approaching chance), and maintains cycle SSIM  $> 0.92$  across both translation directions. Rigorously controlled ablation, including bootstrapped confidence intervals, Bonferroni correction, and Cohen’s  $d$  effect sizes, confirms that self-attention provides a large, statistically reliable benefit ( $d=1.13$ – $1.32$ ) specifically for the harder heterogeneous-to-homogeneous translation direction, at only 3.4% parameter overhead. This combination of principled motivation, architectural efficiency, and rigorous evaluation establishes SA-CycleGAN-2.5D as a strong baseline for future work in multi-center neuroimaging harmonization.

## Code and Data Availability

Source code, pretrained model weights, training scripts, and evaluation pipelines are publicly available at <https://github.com/ishrith-gowda/NeuroScope>. The repository includes: (1) full training code with all six loss components and the 2.5D tri-planar SliceEncoder; (2) evaluation scripts reproducing all reported metrics (MMD, domain classifier, radiomics CCC/ICC); and (3) preprocessing utilities for BraTS/UPenn-GBM cohort preparation. Experiments use publicly available datasets: BraTS (<https://www.synapse.org/brats>) and UPenn-GBM (<https://wiki.cancerimagingarchive.net>).

## References

- [1] Jean-Philippe Fortin, Drew Parker, Birkan Tunç, Takanori Watanabe, Mark A. Elliott, Kosha Ruparel, David R. Roalf, Theodore D. Satterthwaite, Ruben C. Gur, Raquel E. Gur, Robert T. Schultz, Russell T. Shinohara, and Danielle S. Bassett. Harmonization of multi-site diffusion tensor imaging data. *NeuroImage*, 161:149–170, 2017. doi:10.1016/j.neuroimage.2017.08.047.

- [2] Shai Ben-David, John Blitzer, Koby Crammer, Alex Kulesza, Fernando Pereira, and Jennifer Wortman Vaughan. A theory of learning from different domains. *Machine Learning*, 79(1-2):151–175, 2010. doi:10.1007/s10994-009-5152-4.
- [3] Holger R. Roth, Le Lu, Ari Seff, Kevin M. Cherry, Joanne Hoffman, Shijun Wang, Jiamin Liu, Evrim Turkbey, and Ronald M. Summers. A new 2.5D representation for lymph node detection using random sets of deep convolutional neural network observations. In *Medical Image Computing and Computer-Assisted Intervention – MICCAI 2014*, volume 8673 of *Lecture Notes in Computer Science*, pages 520–527. Springer, Cham, 2014. doi:10.1007/978-3-319-10404-1\_65.
- [4] Han Zhang, Ian Goodfellow, Dimitris Metaxas, and Augustus Odena. Self-attention generative adversarial networks. In *Proceedings of the International Conference on Machine Learning (ICML)*, pages 7354–7363, 2019.
- [5] Sanghyun Woo, Jongchan Park, Joon-Young Lee, and In So Kweon. CBAM: convolutional block attention module. In *European Conference on Computer Vision (ECCV)*, volume 11211 of *Lecture Notes in Computer Science*, pages 3–19. Springer, Cham, 2018. doi:10.1007/978-3-030-01234-2\_1.
- [6] W. Evan Johnson, Cheng Li, and Ariel Rabinovic. Adjusting batch effects in microarray expression data using empirical Bayes methods. *Biostatistics*, 8(1):118–127, 2007. doi:10.1093/biostatistics/kxj037.
- [7] Jean-Philippe Fortin, Nicholas Cullen, Yvette I. Sheline, Warren D. Taylor, Irem Aselcioglu, Philip A. Cook, Phil Adams, Crystal Cooper, Maurizio Fava, Patrick J. McGrath, Melvin McInnis, Mary L. Phillips, Madhukar H. Trivedi, Myrna M. Weissman, and Russell T. Shinohara. Harmonization of cortical thickness measurements across scanners and sites. *NeuroImage*, 167:104–120, 2018. doi:10.1016/j.neuroimage.2017.11.024.
- [8] Andrew A. Chen, Joanne C. Beer, Nicholas J. Tustison, Philip A. Cook, Russell T. Shinohara, and Haochang Shou. Removal of scanner effects in covariance improves multivariate pattern analysis in neuroimaging data. *NeuroImage*, 277:120011, 2023. doi:10.1016/j.neuroimage.2023.120011.
- [9] Blake E. Dewey, Can Zhao, Jacob C. Reinhold, Aaron Carass, Kathryn C. Fitzgerald, Elias S. Sotirchos, Shiv Saidha, Jiwon Oh, Dzung L. Pham, Peter A. Calabresi, Peter C. M. van Zijl, and Jerry L. Prince. DeepHarmony: a deep learning approach to contrast harmonization across scanner changes. *Magnetic Resonance Imaging*, 64:160–170, 2019. doi:10.1016/j.mri.2019.05.041.
- [10] Ian Goodfellow, Jean Pouget-Abadie, Mehdi Mirza, Bing Xu, David Warde-Farley, Sherjil Ozair, Aaron Courville, and Yoshua Bengio. Generative adversarial nets. In *Advances in Neural Information Processing Systems*, volume 27, pages 2672–2680, 2014.
- [11] Jun-Yan Zhu, Taesung Park, Phillip Isola, and Alexei A. Efros. Unpaired image-to-image translation using cycle-consistent adversarial networks. In *Proceedings of the IEEE International Conference on Computer Vision (ICCV)*, pages 2223–2232, 2017. doi:10.1109/ICCV.2017.244.
- [12] Gourav Modanwal, Adithya Vellal, Meera Bhatt, Roberta M. Strigel, Christopher C. Conlin, Ji Wu, Barry E. Gillan, Maryellen C. Mahoney, Elizabeth S. Burnside, and Nikita Monga. MRI image harmonization using cycle-consistent generative adversarial network. In *Proceedings of SPIE Medical Imaging*, volume 11314, page 1131413, 2020. doi:10.1117/12.2551301.
- [13] Fenqiang Zhao, Shunren Xia, Zhengwang Wu, Dongrong Duan, Li Wang, Weili Lin, John H. Gilmore, Dinggang Shen, and Gang Li. Harmonization of infant cortical thickness using surface-to-surface cycle-consistent adversarial networks. In *Medical Image Computing and Computer Assisted Intervention – MICCAI 2019*, volume 11767 of *Lecture Notes in Computer Science*, pages 475–483. Springer, Cham, 2019. doi:10.1007/978-3-030-32251-9\_52.
- [14] Wenjie Luo, Yujia Li, Raquel Urtasun, and Richard Zemel. Understanding the effective receptive field in deep convolutional neural networks. In *Advances in Neural Information Processing Systems (NeurIPS)*, pages 4898–4906, 2016.
- [15] Taesung Park, Alexei A. Efros, Richard Zhang, and Jun-Yan Zhu. Contrastive learning for unpaired image-to-image translation. In *European Conference on Computer Vision (ECCV)*, volume 12354 of *Lecture Notes in Computer Science*, pages 319–345. Springer, Cham, 2020. doi:10.1007/978-3-030-58545-7\_19.
- [16] Lianrui Zuo, Blake E. Dewey, Yihao Liu, Yufan He, Scott D. Newsome, Ellen M. Mowry, Susan M. Resnick, Jerry L. Prince, and Aaron Carass. Unsupervised MR harmonization by learning disentangled representations using information bottleneck theory. *NeuroImage*, 243:118569, 2021. doi:10.1016/j.neuroimage.2021.118569.

- [17] Lianrui Zuo, Aaron Carass, Blake E. Dewey, Yufan He, Yihao Liu, Ellen M. Mowry, Scott D. Newsome, Susan M. Resnick, and Jerry L. Prince. HACA3: a unified approach for multi-site MR image harmonization. *Computerized Medical Imaging and Graphics*, 109:102285, 2023. doi:10.1016/j.compmedimag.2023.102285.
- [18] Nicola K. Dinsdale, Mark Jenkinson, and Ana I. L. Namburete. Deep learning-based unlearning of dataset bias for MRI harmonisation and confound removal. *NeuroImage*, 228:117689, 2021. doi:10.1016/j.neuroimage.2020.117689.
- [19] Jieneng Chen, Yongyi Lu, Qihang Yu, Xiangde Luo, Ehsan Adeli, Yan Wang, Le Lu, Alan L. Yuille, and Yuyin Zhou. TransUNet: transformers make strong encoders for medical image segmentation. *arXiv preprint arXiv:2102.04306*, 2021.
- [20] Hu Cao, Yueyue Wang, Joy Chen, Dongsheng Jiang, Xiaopeng Zhang, Qi Tian, and Manning Wang. Swin-Unet: Unet-like pure transformer for medical image segmentation. In *European Conference on Computer Vision Workshops*, pages 205–218. Springer, Cham, 2022. doi:10.1007/978-3-031-25066-8\_9.
- [21] Olaf Ronneberger, Philipp Fischer, and Thomas Brox. U-Net: convolutional networks for biomedical image segmentation. In *Medical Image Computing and Computer Assisted Intervention – MICCAI 2015*, volume 9351 of *Lecture Notes in Computer Science*, pages 234–241. Springer, Cham, 2015. doi:10.1007/978-3-319-24574-4\_28.
- [22] Dmitry Ulyanov, Andrea Vedaldi, and Victor Lempitsky. Instance normalization: the missing ingredient for fast stylization, 2016.
- [23] Phillip Isola, Jun-Yan Zhu, Tinghui Zhou, and Alexei A. Efros. Image-to-image translation with conditional adversarial networks. In *Proceedings of the IEEE Conference on Computer Vision and Pattern Recognition (CVPR)*, pages 1125–1134, 2017. doi:10.1109/CVPR.2017.632.
- [24] Takeru Miyato, Toshiki Kataoka, Masanori Koyama, and Yuichi Yoshida. Spectral normalization for generative adversarial networks. In *International Conference on Learning Representations (ICLR)*, 2018.
- [25] Xudong Mao, Qing Li, Haoran Xie, Raymond Y. K. Lau, Zhen Wang, and Stephen Paul Smolley. Least squares generative adversarial networks. In *Proceedings of the IEEE International Conference on Computer Vision (ICCV)*, pages 2794–2802, 2017. doi:10.1109/ICCV.2017.304.
- [26] Zhou Wang, Alan C. Bovik, Hamid R. Sheikh, and Eero P. Simoncelli. Image quality assessment: from error visibility to structural similarity. *IEEE Transactions on Image Processing*, 13(4):600–612, 2004. doi:10.1109/TIP.2003.819861.
- [27] Diederik P. Kingma and Jimmy Ba. Adam: A method for stochastic optimization. In Yoshua Bengio and Yann LeCun, editors, *International Conference on Learning Representations (ICLR)*, 2015. URL <https://arxiv.org/abs/1412.6980>.
- [28] Bjoern H. Menze, Andras Jakab, Stefan Bauer, Jayashree Kalpathy-Cramer, Keyvan Farahani, Justin Kirby, Yuliya Burren, Nicole Porz, Johannes Slotboom, Roland Wiest, Levente Lenczi, Elizabeth Gerstner, Marc-Andre Weber, Tal Arbel, Brian B. Avants, Nicholas Ayache, Patricia Buendia, D. Louis Collins, Nicolas Cordier, Jason J. Corso, Antonio Criminisi, Tilak Das, Hervé Delingette, Çağatay Demiralp, Christopher R. Durst, Michel Dojat, Senan Doyle, Joana Festa, Florence Forbes, Ezequiel Geremia, Ben Glocker, Polina Golland, Xiaotao Guo, Andac Hamamci, Khan M. Iftekharuddin, Raj Jena, Nigel M. John, Ender Konukoglu, Danial Lashkari, José Antonio Mariz, Raphael Meier, Sérgio Pereira, Doina Precup, Stephen J. Price, Tammy Riklin Raviv, Syed M. S. Reza, Michael Ryan, Duygu Sarikaya, Lawrence Schwartz, Hoo-Chang Shin, Jamie Shotton, Carlos A. Silva, Nuno Sousa, Nagesh K. Subbanna, Gabor Szekely, Thomas J. Taylor, Owen M. Thomas, Nicholas J. Tustison, Gozde Unal, Flor Vasseur, Max Wintermark, Dong Hye Ye, Liang Zhao, Binsheng Zhao, Darko Zikic, Marcel Prastawa, Mauricio Reyes, and Koen Van Leemput. The multimodal brain tumor image segmentation benchmark (BRATS). *IEEE Transactions on Medical Imaging*, 34(10):1993–2024, 2015. doi:10.1109/TMI.2014.2377694.
- [29] Spyridon Bakas, Hamed Akbari, Aristeidis Sotiras, Michel Bilello, Martin Rozycki, Justin S. Kirby, John B. Freymann, Keyvan Farahani, and Christos Davatzikos. Advancing The Cancer Genome Atlas glioma MRI collections with expert segmentation labels and radiomic features. *Scientific Data*, 4:170117, 2017. doi:10.1038/sdata.2017.117.
- [30] Spyridon Bakas, Chiharu Sako, Hamed Akbari, Michel Bilello, Xiao Da, Sana Rustam, Allison McGill, Tom Kirschbaum, Jeffrey D. Rudie, and Christos Davatzikos. The University of Pennsylvania glioblastoma (UPenn-GBM) cohort: advanced MRI, clinical, genomics, & radiomics. *Scientific Data*, 9(1):453, 2022. doi:10.1038/s41597-022-01560-7.

- [31] Nicholas J. Tustison, Brian B. Avants, Philip A. Cook, Yuanjie Zheng, Alexander Egan, Paul A. Yushkevich, and James C. Gee. N4ITK: improved N3 bias correction. *IEEE Transactions on Medical Imaging*, 29(6):1310–1320, 2010. doi:10.1109/TMI.2010.2046908.
- [32] Fabian Isensee, Marianne Schell, Irada Pflueger, Gianluca Brugnara, David Bonekamp, Ulf Neuberger, Antje Wick, Heinz-Peter Schlemmer, Sabine Heiland, Wolfgang Wick, Martin Bendszus, Klaus H. Maier-Hein, and Philipp Kickingereder. Automated brain extraction of multisequence MRI using artificial neural networks. *Human Brain Mapping*, 40(17):4952–4964, 2019. doi:10.1002/hbm.24750.
- [33] Torsten Rohlfing, Natalie M. Zahr, Edith V. Sullivan, and Adolf Pfefferbaum. The SRI24 multi-channel atlas of normal adult human brain structure. *Human Brain Mapping*, 31(5):798–819, 2010. doi:10.1002/hbm.20906.
- [34] Richard Zhang, Phillip Isola, Alexei A. Efros, Eli Shechtman, and Oliver Wang. The unreasonable effectiveness of deep features as a perceptual metric. In *Proceedings of the IEEE Conference on Computer Vision and Pattern Recognition (CVPR)*, pages 586–595, 2018. doi:10.1109/CVPR.2018.00068.
- [35] Arthur Gretton, Karsten M. Borgwardt, Malte J. Rasch, Bernhard Schölkopf, and Alexander Smola. A kernel two-sample test. *Journal of Machine Learning Research*, 13:723–773, 2012.
- [36] Kaiming He, Xiangyu Zhang, Shaoqing Ren, and Jian Sun. Deep residual learning for image recognition. In *Proceedings of the IEEE Conference on Computer Vision and Pattern Recognition (CVPR)*, pages 770–778, 2016. doi:10.1109/CVPR.2016.90.
- [37] Lawrence I-Kuei Lin. A concordance correlation coefficient to evaluate reproducibility. *Biometrics*, 45(1):255–268, 1989. doi:10.2307/2532051.
- [38] Patrick E. Shrout and Joseph L. Fleiss. Intraclass correlations: uses in assessing rater reliability. *Psychological Bulletin*, 86(2):420–428, 1979. doi:10.1037/0033-2909.86.2.420.
- [39] Alex Zwanenburg, Martin Vallières, Mahmoud A. Abdalah, Hugo J. W. L. Aerts, Vincent Andrearczyk, Aditya Apte, Saeed Ashrafinia, Spyridon Bakas, Roelof J. Beukinga, Ronald Boellaard, Marta Bogowicz, Luca Boldrini, Irène Buvat, Gary J. R. Cook, Christos Davatzikos, Adrien Depeursinge, Marie-Charlotte Desseroit, Nicola Dinapoli, Cu Vinh Dinh, Sebastian Echeagaray, Issam El Naqa, Andrey Y. Fedorov, Roberto Gatta, Robert J. Gillies, Vicky Goh, Michael Götz, Matthias Guckenberger, Sang Mo Ha, Mathieu Hatt, Fabian Isensee, Philippe Lambin, Stefan Leger, Ralph T. H. Leijenaar, Jacopo Lenkiewicz, Fiona Lippert, Are Losnegård, Klaus H. Maier-Hein, Olivier Morin, Henning Müller, Sandy Napel, Christophe Nioche, Fanny Orhac, Sarthak Pati, Elisabeth A. G. Pfaehler, Arman Rahmim, Arvind U. K. Rao, Jonas Scherer, Md Minhazul Siddique, Nanna M. Sijtsema, Jairo Socarras Fernandez, Emiliano Spezi, Roel J. H. M. Steenbakkens, Stephanie Tanadini-Lang, Daniela Thorwarth, Esther G. C. Troost, Taman Upadhaya, Vincenzo Valentini, Lisanne V. van Dijk, Joost van Griethuysen, Floris H. P. van Velden, Philip Whybra, Christoph Richter, and Steffen Löck. The image biomarker standardization initiative: standardized quantitative radiomics for high-throughput image-based phenotyping. *Radiology*, 295(2):328–338, 2020. doi:10.1148/radiol.2020191145.
- [40] Laurens van der Maaten and Geoffrey Hinton. Visualizing data using t-SNE. *Journal of Machine Learning Research*, 9(86):2579–2605, 2008. URL <https://www.jmlr.org/papers/v9/vandermaaten08a.html>.
- [41] Joost J. M. van Griethuysen, Andriy Fedorov, Chintan Parmar, Ahmed Hosny, Nicole Aucoin, Vivek Narayan, Regina G. H. Beets-Tan, Jean-Christophe Fillon-Robin, Steve Pieper, and Hugo J. W. L. Aerts. Computational radiomics system to decode the radiographic phenotype. *Cancer Research*, 77(21):e104–e107, 2017. doi:10.1158/0008-5472.CAN-17-0339.
- [42] Yunjey Choi, Minje Choi, Munyoung Kim, Jung-Woo Ha, Sunghun Kim, and Jaegul Choo. StarGAN: unified generative adversarial networks for multi-domain image-to-image translation. In *Proceedings of the IEEE Conference on Computer Vision and Pattern Recognition (CVPR)*, pages 8789–8797, 2018. doi:10.1109/CVPR.2018.00916.